PHYSICAL REVIEW B **108**, 085429 (2023)

# Origin of bound exciton emission in CVD-grown monolayer MoS$_2$

Kishore K. Madapu[1,*] C. Abinash Bhuyan,[2] and Sandip Dhara[1,2,†]
[1]*Surface and Sensors Studies Division, Materials Science Group, Indira Gandhi Centre for Atomic Research, Kalpakkam-603 102, India*
[2]*Indira Gandhi Centre for Atomic Research, A CI of Homi Bhabha National Institute, Kalpakkam 603102, Tamil Nadu, India*

(Received 20 February 2023; revised 4 August 2023; accepted 8 August 2023; published 25 August 2023)

Chemical vapor deposition (CVD) is one of the prominent techniques to realize the device-grade monolayer MoS$_2$ (1L-MoS$_2$). Thus, it is important to understand the defects in CVD grown 1L-MoS$_2$ to develop the 1L-MoS$_2$–based optoelectronic devices. In this work, we established the origin of defect-bound exciton emission in CVD-grown 1L-MoS$_2$ using low-temperature photoluminescence (PL) spectroscopy. So far, the role of substrate in bound exciton emission of 1L-MoS$_2$ has largely been overlooked. Here, we adopted an innovative dry detachment method to delineate the effect of substrate-borne impurities on bound exciton emission. The bound exciton emission was completely absent in the detached 1L-MoS$_2$ flake. The role of substrate-borne impurities was established using the Raman and PL spectroscopies by qualitatively analyzing the carrier density in the film before and after detachment. Kelvin probe force microscopy was employed to gauge surface-potential change after detachment. The work function of 1L-MoS$_2$ was found to be increased by 90 meV after the detachment. In addition, the bound exciton emission of as-grown 1L-MoS$_2$ was compared for wet- and surface-energy assisted transferred 1L-MoS$_2$ flakes. We also found that the strength of the bound exciton emission is dependent on the heat-dissipating area of the 1L-MoS$_2$ flake.

DOI: 10.1103/PhysRevB.108.085429

## I. INTRODUCTION

Since the last decade, semiconducting two-dimensional (2D) transitional-metal dichalcogenides (TMDs) have attracted significant attention because of their fascinating optical properties [1–4]. Especially, having a sizable direct band gap is an advantage over graphene [2,3]. Among the other semiconducting 2D TMDs, molybdenum disulfide (MoS$_2$) is the most explored material. The photoluminescence (PL) quantum yield of the monolayer MoS$_2$ (1L-MoS$_2$) is four-orders higher than its bulk counterpart [2]. Moreover, excitons in monolayer TMDs have one-order higher binding energies than conventional quantum-well structures [5]. The weak dielectric screening of electron-hole Coulomb interaction, originating from the atomic-scale thickness and variation in the dielectric environment, is the reason for the high binding energies of excitons [6,7]. The presence of excitons at room temperature opens interesting exciton physics to explore and find applications in the field of optoelectronic devices [8]. In line with this, the existence of other quasiparticles, such as trions (charged exciton) [9] and biexcitons [5,10–13], further enriched the interest in these materials. In addition, 1L-MoS$_2$ has also been explored for several optoelectronic applications such as photodetectors [14–16], transistors [17,18], solar cells [19], and gas sensor applications [20].

The room-temperature (RT) PL spectrum of 1L-MoS$_2$ shows the quasiparticle emission and is influenced by the intrinsic defects [21–24], strain [25], substrate [26,27], surface adsorbents [9,28–30], local temperature [31], and excitation energy [32]. Even though it has been more than a decade since the realization of 1L-MoS$_2$, reports on low-temperature exciton properties are very few [13,21,33–38]. It is worth mentioning that the effect of defects on the exciton landscape can be thoroughly understood by the low-temperature PL studies. Including the early reports, most of the low-temperature studies are concentrated on mechanically exfoliated 1L-MoS$_2$ [13,21,33–36]. In this context, exploration of exciton behavior at low temperatures in the case of 1L-MoS$_2$ grown by chemical vapor deposition (CVD) is rare [37,38]. It is worth mentioning that the synthesis of high-quality, device-grade, and large-area 1L-MoS$_2$ is plausible only via the CVD method [31,39]. Thus, it is inevitable to establish the defect-related emission and its effect on the exciton landscape in CVD-grown 1L-MoS$_2$ as the performance of the devices is significantly influenced by defects [40]. However, defects in CVD-grown 1L-MoS$_2$ are fundamentally different from mechanically exfoliated 1L-MoS$_2$, especially substrate-induced defects [26].

In early reports, low-temperature exciton properties were explored on mechanically exfoliated 1L-MoS$_2$. Korn *et al.* [33] found that the PL spectrum of 1L-MoS$_2$ at cryogenic temperatures (4.5 K) was different from the RT PL spectrum. A broad peak was observed at 90 meV below the free-exciton emission peak. The broad peak in PL spectra was ascribed to bound exciton emission [33]. Plechinger *et al.* [34] found that the bound exciton emission was suppressed entirely when the 1L-MoS$_2$ flake was covered with the oxide layers. Hence, it was speculated that the bound exciton emission might be originated from the surface-adsorbed impurities [34]. In another independent work, Tongay *et al.* [21] correlated the bound exciton emission with excitons bound to S (anion) vacancy defects, where the anion vacancies were created by

---

[*] madupu@igcar.gov.in
[†] dhara@igcar.gov.in

$\alpha$-particle irradiation. Interestingly, Saigal and Ghosh [35] evidenced two distinct bound exciton emission peaks below the free-exciton emission peak. In their report, the origin of bound exciton emissions was attributed to the excitons bound to single- ($V_S$) and double ($V_{2S}$)-sulfur vacancies [35]. However, in all these cases, the bound exciton emission was not explicitly observed above 120 K [33]. In this context, Pandey *et al.* observed the disappearance of bound exciton emission above 50 K [13]. The defect-bound exciton emission was observed even at room temperature in plasma-treated monolayer $MoS_2$ flakes [22]. Recently, Verhagen *et al.* [37] utilized low-temperature PL spectroscopy to evaluate the defects in CVD-grown 1L-$MoS_2$. The contribution of bound exciton emission was increased with decreasing of sample temperature. At ultralow temperatures (~4 K), the PL spectrum was largely dominated by the bound exciton emission. In this case also, the bound exciton emission is attributed to the presence of $V$s and $V_{2S}$. The increase of bound exciton emission contribution with the lowering of temperature was attributed to the reduced interaction with phonons. In contrast, bound exciton emission was not found in the case of wet-transferred 1L-$MoS_2$ samples, and it was attributed to the passivation of S vacancies by KOH during the transfer process [37]. In earlier reports, the effect of substrate-borne defects on bound exciton emission was underestimated compared to the intrinsic defects and surface-adsorbed impurities. In addition, the impact of local temperature on bound exciton emission has been overlooked so far. In this context, CVD-grown 1L-$MoS_2$ is more susceptible to interface defects than exfoliated samples. The exclusive substrate effect on bound exciton emission can only be delineated by transferring the CVD-grown 1L-$MoS_2$ to another substrate. However, the conventional transfer methods may modify the 1L-$MoS_2$ inherent properties [41]. Thus, a true dry-transfer method is required to avoid any polymer-induced effects.

In this paper, low-temperature PL spectroscopy analysis was carried out on CVD-grown 1L-$MoS_2$. An innovative dry-detachment method based on a differential thermal expansion coefficient was adopted to delineate the origin of bound exciton emission. The bound exciton emission of CVD-grown 1L-$MoS_2$ was found to originate from the $SiO_2/MoS_2$ interface defects. The role of substrate-borne impurities or interface defects was confirmed by the Raman spectroscopic analysis and was further corroborated by surface-potential measurements using Kelvin probe force microscopy (KPFM). The bound exciton emission of as-grown 1L-$MoS_2$ was compared for wet- and surface-energy assisted transferred 1L-$MoS_2$. In addition, we found that the contribution of bound exciton emission varies with the heat-dissipating area of 1L-$MoS_2$.

## II. EXPERIMENTAL METHODS

Samples of 1L-$MoS_2$ were grown on thermally oxide $SiO_2$(300 nm)/Si and sapphire ($c$-$Al_2O_3$) substrates via the CVD method using a three-zone furnace. The $MoO_3$ (99.99%, Sigma-Aldrich) and S (99.9%, Sigma-Aldrich) powders were used as the precursor materials. Alumina boats with precursor materials were kept in a 1-inch quartz tube. The S powder was evaporated at 165 °C in the first zone of the furnace. The $MoO_3$ powder was kept in the third zone and maintained at 700 °C temperature during the growth process. The second zone was maintained at 200 °C during the growth. All the zones reached the set temperature at the same time, 40 min. The growth time was 20 min. A constant flow (50 sccm) of ultrahigh pure Ar was maintained during the growth process, which flows from the first to the third zone. The substrates were kept over the $MoO_3$ powder. High-quality 1L-$MoS_2$ samples were regularly produced in our laboratory with a similar approach [31,41,42]. As-grown 1L-$MoS_2$ flakes were transferred onto other $SiO_2$/Si and sapphire substrates by two well-established methods, such as poly(methyl methacrylate) (PMMA)-assisted wet-transfer method [41] and surface-energy assisted transfer method using polystyrene (PS) polymer [43].

Raman and PL measurements were carried out using a micro-Raman spectrometer (Renishaw, UK) with the excitation of a 532 nm laser. Raman scattering was dispersed through 2400 grooves/mm grating, whereas PL emission was dispersed through 1800 grooves/mm grating. The Raman-scattered light and PL emission were collected using a thermoelectric cooled charge-coupled device detector. The low-temperature measurements were carried out using the liquid nitrogen-based low-temperature stage (TS 92, Linkam). The low-temperature stage was continuously purged with $N_2$ gas during the PL measurements. The temperature values mentioned in the present work indicate the temperature of the sample stage. Unless otherwise stated, low-temperature PL spectra were acquired using a long working distance 100× objective lens (numerical aperture, NA-0.74) with a laser power of 0.02 mW. Room-temperature (RT) Raman and PL measurements were recorded using the 100× objective lens (NA-0.85) with a laser power of 0.103 mW. Topography analysis was carried out using the tuning-fork based atomic force microscopy (AFM), whereas a beam-bounce module was used for the KPFM measurements (MV 4000, Nanonics, Israel). The normal-mode feedback mechanism was used for AFM and KPFM measurements. In the present study, Au-coated Si tip (radius ~25 nm) with a resonance frequency of ~56 kHz was used for the KPFM measurements.

## III. RESULTS

### A. Bound exciton emission and effect of heat-dissipating area

Initially, as-grown samples were inspected by optical microscopy. The as-grown samples contained flakes of triangular shapes as well as large-area regions. In the present study, the flake area $\geqslant$500 μm$^2$ is considered as the large-area flake. Figure S1 in the Supplemental Material (SM) [44] shows the optical images of 1L-$MoS_2$ flakes grown on $SiO_2$/Si and sapphire substrates. The AFM and Raman spectroscopy analysis confirmed the grown flakes were monolayers [31,42]. Low-temperature PL analysis was carried out to understand the defects in the CVD-grown 1L-$MoS_2$ samples. For this analysis, two flake areas were selected, i.e., a small area ($\leqslant$30 μm$^2$) and a large area ($\geqslant$500 μm$^2$). Figure 1 shows the typical PL spectrum of small-area [Fig. 1(a)] and large-area [Fig. 1(b)] flakes recorded at 77 K. Interestingly, the PL spectra are significantly different from each other. A similar kind of observation was made on the other flakes which were grown

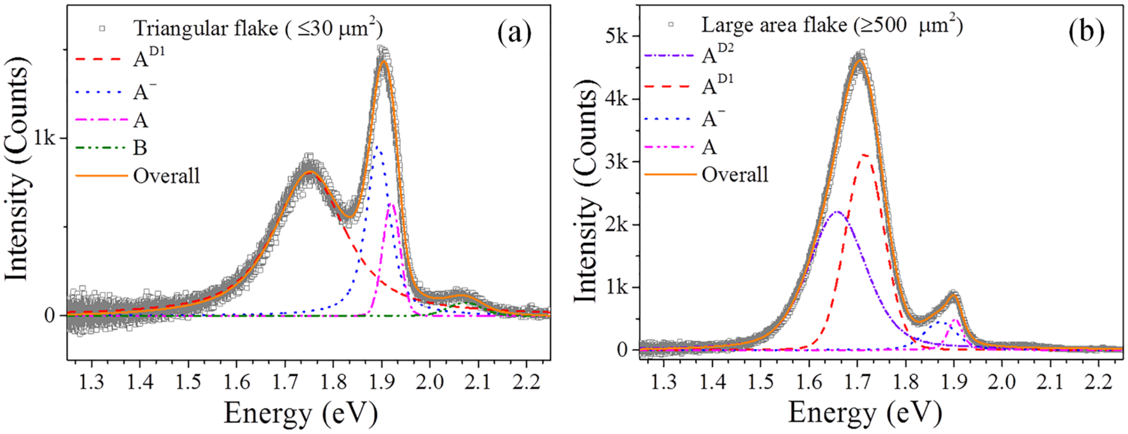

FIG. 1. Low-temperature PL analysis of 1L-MoS$_2$ grown on SiO$_2$ substrate by CVD method. PL spectra were recorded by maintaining sample-stage temperature at 77 K. PL spectrum of (a) small-flake area ($\leqslant$30 μm$^2$) and (b) large-flake area ($\geqslant$500 μm$^2$) flakes. Defect-bound exciton emission was observed for both cases with different degrees of contribution. Bound exciton emission of large-area flake was deconvoluted into $A^{\mathrm{D1}}$ and $A^{\mathrm{D2}}$, whereas $A^{\mathrm{D2}}$ peak is absent for small-area flake. Active regions of PL spectra are fitted with mixed Gaussian-Lorentzian function.

on other SiO$_2$ substrates (Fig. S2 [44]). The low-temperature PL spectra were well fitted with mixed Gaussian-Lorentzian functions (Fig. 1) [22,44]. The fitting results indicate the presence of free excitons ($A$ exciton, and $B$ exciton), trion ($A^-$), and bound excitons. The bound exciton emission is observed when the free excitons are trapped at defects in the system. However, the bound exciton emission of the large-area flake is the convolution of two peaks, which are represented as $A^{\mathrm{D1}}$ and $A^{\mathrm{D2}}$. The observation of two bound exciton emissions is in accordance with earlier reports [35]. Surprisingly, we failed to observe the $A^{\mathrm{D2}}$ emission in the case of the small-area flake. In addition, the bound exciton emission contribution dominated the PL spectrum of large-area flakes, whereas it was low in the case of small-area flakes. Verhagen *et al.* reported that the bound exciton emission dominated only at ultralow temperatures (4 K) [37]. In contrast, we found that the bound exciton emission dominated even at 100 K in the case of large-area flake.

Power-dependent PL studies were conducted to understand the absence of the $A^{\mathrm{D2}}$ peak in the PL spectra of small-area flakes. PL spectra of small- [Fig. 2(a)] and large-area [Fig. 2(b)] flakes were recorded at 77 K with different laser powers. In both cases, the contribution of $A$-exciton and trions increased as the laser power increased, and the concomitantly bound exciton contribution reduced. However, the variation of overall PL shape with increased laser power was more noticeable in large-area flake [Fig. 2(b)]. To be precise, the domination of bound exciton emission is substantially suppressed with increased laser power. It was also found that the $A^{\mathrm{D2}}$ peak was absent with high laser powers ($\geqslant$0.204 mW). Conversion of the bound exciton to free excitons and trions is the reason for suppressing bound exciton emission and the disappearance of $A^{\mathrm{D2}}$. The conversion of the bound excitons with increased laser power is attributed to their low thermal stability [33]. Figure 2(c) shows the variation in the integrated intensity ratio of excitons $[I(A^-) + I(A)]$ and bound exciton $[I(A^{\mathrm{D1}}) + I(A^{\mathrm{D2}})]$ emission with laser power. It was found that the conversion rate is higher for the small-area flake (slope, $m = 3.48$), whereas the value was low for the large-area flake ($m = 1.07$). This difference is attributed to the substantial rise in the local temperature of small-area flakes, which enhances the conversion of bound excitons to free excitons. The effect of laser-induced heat is discussed in the subsequent paragraph. Interestingly, the shape of the large-area flake PL spectrum with 1.02 mW laser power was similar to the PL spectrum of the small-area flake with 0.204 mW laser power. These observations suggest that similar conditions must have prevailed in large-area flakes with high laser power akin to small ones with low laser power. The absence of $A^{\mathrm{D2}}$ peak, even for low laser power, for the small-area flake is attributed to the significant rise in local temperature because of the less heat-dissipating area. We have already reported that large-area flakes efficiently dissipate the laser-induced heat [31,32]. Thus, the relative intensity of bound exciton emission and presence of $A^{\mathrm{D2}}$ peak is dependent on the laser power of excitation, i.e., local temperature. In addition, the disappearance of the $A^{\mathrm{D2}}$ peak with laser power reveals that the $A^{\mathrm{D2}}$ peak is more sensitive to local temperature. However, previously it was also reported that the bound exciton is dependent on the defect density [21,22]. Thus, the present results reveal that the strength of bound exciton emission depends not only on the defect density but also on the heat-dissipating area. The $A$- and $A^-$-peak positions were redshifted with increased laser power in the case of small-area flake [Fig. 2(d)]. In contrast, large-area flakes showed a negligible change with laser power [Fig. 2(e)]. The redshift in exciton peak position ($A$ and $A^-$) is attributed to the rise in local temperature due to less heat-dissipating area, whereas it is negligible in the case of the large area due to efficient heat dissipation [31,32]. These observations further substantiate the fact that heat dissipation is indeed efficient in large-area flakes. However, the $A^{\mathrm{D1}}$ peak was blueshifted with increased laser power for both cases [Figs. 2(d) and 2(e)]. The blueshift of $A^{\mathrm{D1}}$ peak is attributed to nonradiative recombination of high binding-energy bound excitons. A reason beyond this is yet to be understood. It is worth mentioning that the large width of bound exciton emission indicates the availability of different binding-energy sites [33]. Figure S3 shows the low-temperature power-dependent

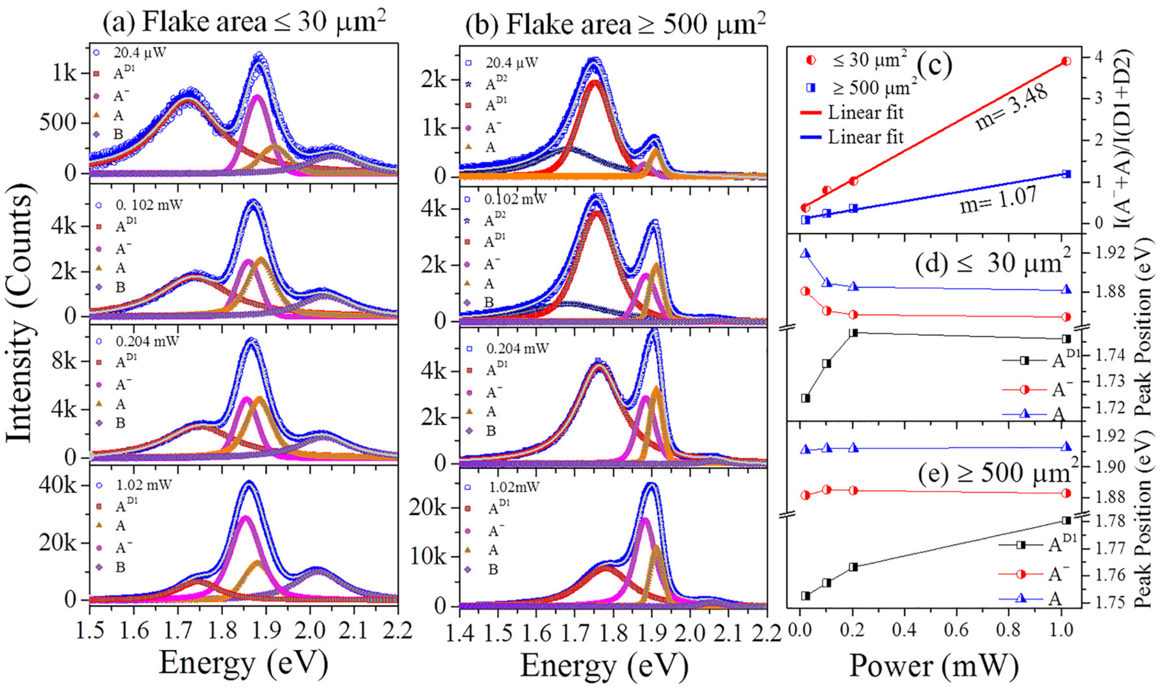

FIG. 2. Low-temperature power-dependent PL analysis of (a) small- and (b) large-area flakes. Power-dependent PL measurements were carried out at sample-stage temperature of 77 K. (c) Variation of integrated intensity ratio $A$ and $A^-$ and defect bound exciton emission ($A^{D1}+A^{D2}$), [$I(A+A^-)/I(A^{D1}+A^{D2})$], with laser power. Variation of peak position of $A^-$, $A$, and $A^{D1}$ with laser powers for (d) small-area flake and (e) large-area flakes. Active regions of PL spectra are fitted with mixed Gaussian-Lorentzian function.

PL studies of other small- and large-area flakes with more data points. In this case, a similar trend was also observed [44].

We further carried out the temperature-dependent PL measurements on large- and small-area flakes. Figures S4(a) and S4(b) show the temperature-dependent PL spectra of small-area and large-area 1L-$MoS_2$ flakes, respectively [44]. The domination of bound exciton emission was observed up to 100 K in the large-area flake. Bound exciton emission disappeared above 120 K in the case of small-area flakes in accordance with the literature. In contrast, the $A^{D1}$ peak was observed as a shoulder up to 210 K in a large-area flake. As mentioned earlier, the defect-bound exciton emission is not observed above 120 K in untreated flakes. The contrasting behavior can be understood by considering the local temperature. The local temperature is dependent on the heat-dissipating area of the 1L-$MoS_2$ flake [31,32]. For a particular laser power, the local temperature is different for small- and large-area flakes. The rise in local temperature in the small-area flake is significant because of inefficient heat dissipation. Here, the local temperature is the addition of the sample temperature and the temperature rise caused by laser-induced heat. As the bound exciton emission was sensitive to temperature [33], it disappeared at low temperatures (120 K) in the case of a small-area flake. On the contrary, temperature rise caused by laser-induced heating is negligible for the large-area flake because of efficient heat dissipation. Thus, bound exciton emission is sustained even for higher temperatures (210 K). The same explanation is applicable to the power-dependent results. Thus, observation of defect-bound exciton emission at 210 K in large-area flake is attributed to the reduced laser-induced heating effects because of efficient heat dissipation. The temperature-dependent PL of large-area flakes with peak fitting is presented in Fig. S5 [44]. The temperature-dependent peak positions of bound excitons ($A^{D1}$ and $A^{D2}$), $A$- and $A$, are plotted in Fig. S6 for the large-area flake [44]. Interestingly, the absence of $A^{D2}$ above 90 K reveals its low thermal stability. A similar observation was made in power-dependent PL studies where the effect of heat generation with laser power and dissipation with flake area were considered. Similar to power-dependent studies, $A^{D1}$ was blueshifted with increasing temperature.

### B. Origin of bound exciton emission in CVD-grown monolayer $MoS_2$

In literature, the origin of bound exciton emission was attributed to excitons bound to $V_S$ and $V_{2S}$ [13,21,37]. However, most of the studies were carried out on mechanically exfoliated monolayer flakes [13,21,33–36]. Hitherto, the effect of substrate is overlooked. However, one cannot neglect the effect of the substrate in CVD-grown monolayer flakes because of the strong bonding between the substrate and grown flakes. The substrate-borne impurities create interface defects, which act as charged traps. These charged traps either deplete or accumulate the electrons in the conducting channel. The influence of the charged traps is dependent on screening length. For instance, Na-, H-, and O-dangling bonds are typical $SiO_2$/1L-$MoS_2$ interface charge traps. A detailed discussion is provided in Sec. IV. In this context, the growth of 1L-$MoS_2$ was carried out on a sapphire substrate to elucidate the exclusive substrate effects. A 77 K PL spectrum was acquired from the 1L-$MoS_2$ grown on a sapphire substrate and compared with the PL spectra of the 1L-$MoS_2$ grown on a $SiO_2$ substrate [Fig. 3(a)]. Interestingly, the bound exciton

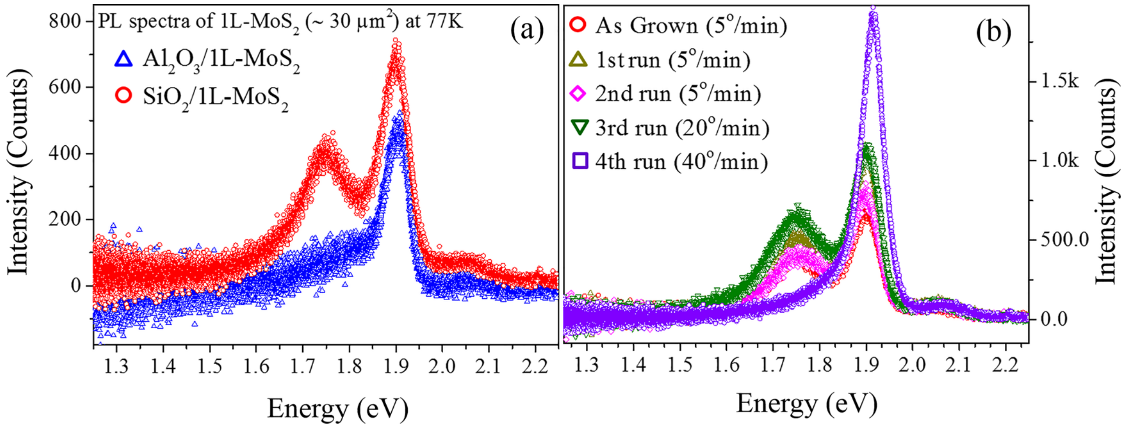

FIG. 3. Role of substrate on defect-bound exciton emission. (a) Comparative PL spectrum of 1L-MoS$_2$ grown on sapphire and SiO$_2$ substrate by CVD. PL spectra recorded at sample-stage temperature of 77 K. (b) Low-temperature PL spectra of as-grown 1L-MoS$_2$ flake (SiO$_2$ substrate) and after heating to RT with different ramp rates of 5, 20, and 40 °C/min.

peak was absent in the case of the 1L-MoS$_2$ grown on a sapphire substrate [Fig. 3(a)]. Thus, it is suggested that the bound exciton emission is limited to 1L-MoS$_2$ flakes grown on SiO$_2$ substrates. Moreover, the absence of bound exciton emission in sapphire-supported flakes reveals the bound exciton emission must be originated from SiO$_2$ substrate-induced defects, as the growth conditions are the same for both substrates. However, observation of bound exciton emission may be possible in 1L-MoS$_2$ grown on sapphire if the growth is carried out in Mo-rich conditions.

As mentioned earlier, the polymer-assisted transfer methods may change the inherent properties of 2D materials [41]. An innovative dry method was adopted to detach grown flakes from the SiO$_2$ substrate to probe the exclusive substrate effects. A one-order difference in the thermal expansion coefficient of MoS$_2$ ($\sim 6 \times 10^{-6}$ K$^{-1}$) [52] and SiO$_2$ ($0.6 \times 10^{-6}$ deg$^{-1}$ at 25 °C) [53] is exploited to detach grown flakes from the substrate. Initially, the sample was cooled down to 77 K with a ramp rate of 5 °C/min. Subsequently, the sample was heated to 300 from 77 K with different ramp rates. Figure 3(b) shows the PL spectra recorded at 77 K after bringing the sample to RT with different ramp rates (5, 20, and 40 °C/min). Here, the sample was cooled down to 77 K with a ramp rate of 5 °C/min for acquiring the PL at 77 K after reaching RT (300 K). For comparison, the low-temperature PL spectrum of as-grown 1L-MoS$_2$ flake was also shown in Fig. 3(b). The defect-bound exciton was clearly observed in the PL spectrum of as-grown flake [Fig. 3(b)]. The bound exciton emission was observed after heating the sample with a ramp rate of 5 °C/min twice. Subsequently, the heating ramp rate was increased to 20 °C/min. In this case, the low-temperature (77 K) PL spectrum was not changed compared to that for the as-grown sample. The heating ramp rate was further increased to 40 °C/min. The bound exciton emission disappeared in the PL spectrum after heating the sample with a ramp rate of 40 °C/min. Here, we have not carried out any chemical treatment to the flake to suppress the bound exciton emission. The only change we made was an increase in the ramp rate of heating. Thus, the origin of the disappearance of bound exciton emission must be related to high ramp-rate heating. The plausible reason for the absence of bound exciton emission is the detachment of 1L-MoS$_2$ flake from the substrate surface. The difference in thermal expansion coefficients of MoS$_2$ and SiO$_2$ leads to a different degree of expansion. One can safely assume that expansion might have occurred only in MoS$_2$ flakes, as the expansion of SiO$_2$ is negligible [54]. The sudden expansion of the 1L-MoS$_2$ flake caused by the high ramp rate leads to the detachment of 1L-MoS$_2$ from SiO$_2$. Hence, the absence of bound exciton emission is attributed to the detachment of 1L-MoS$_2$ flake from the SiO$_2$ substrate. It is also inferred that the bound exciton emission in monolayer MoS$_2$ grown by CVD stems from substrate-borne impurities or interface defects. The above-mentioned detachment process was carried out in the following manner. In a single sample, we selected ten flakes for the observations. Out of ten flakes, 20–30% were detached and retained the structural integrity after the high ramp-rate heating, and the remaining flakes were either broken apart or not detached.

Exciton-peak analysis was carried out before and after the flake detachment to ascertain our assumption. This particular analysis was carried out on another arbitrary flake grown on other SiO$_2$ substrate with similar experimental conditions. As mentioned in the preceding section, the detachment of 1L-MoS$_2$ from the SiO$_2$ was carried out with a high ramp rate (40 °C/min) of heating. Figures 4(a) and 4(b) show the PL spectrum recorded at 77 K before and after the detachment of 1L-MoS$_2$ flake, respectively. Once again, bound exciton emission was absent after detachment [Fig. 4(b)]. The fitting was carried out with mixed Gaussian and Lorentzian functions [44]. The PL spectrum of as-grown (before detachment) flakes is well fitted with four peaks such as $A^{D1}$ (~1.72 eV), $A^-$ (~1.87 eV), $A$ (~1.90 eV), and $B$ (~2.04 eV) excitons [Fig. 4(a)]. However, the PL spectrum of the same flake after detachment is fitted with only three peaks such as $A^-$ (~1.86 eV), $A$ (~1.91 eV), and $B$ (~2.08 eV) [Fig. 4(b)]. The peak positions of $A^-$, $A$, and $B$ were not shifted significantly after detachment. However, the integrated intensities of $A^-$ and $A$ peaks were changed considerably after detachment. PL spectrum of as-grown flake dominated by trion emission. In contrast, free-exciton emission dominated the PL spectrum of the detached flake [Fig. 4(b)]. The integrated intensity ratio

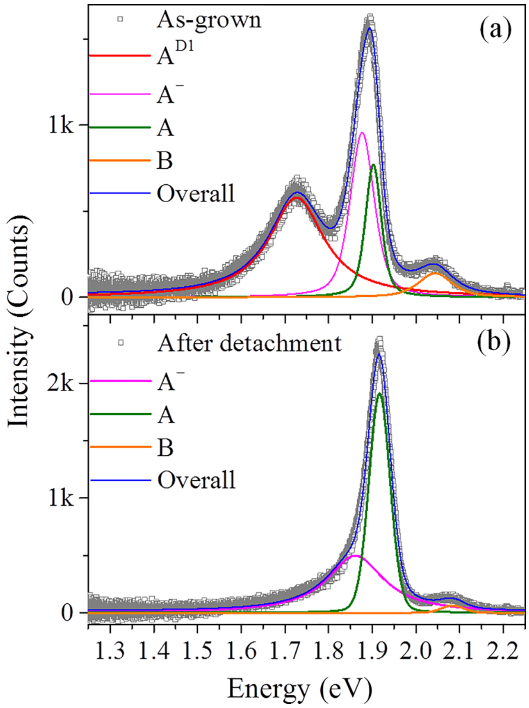

FIG. 4. Exciton-peak analysis of arbitrary 1L-$MoS_2$ flake grown on other $SiO_2$ substrate with same CVD conditions. Measurements were carried out at sample-stage temperature of 77 K. (a) Fitted PL spectrum of as-grown 1L-$MoS_2$. (b) Fitted PL spectrum of 1L-$MoS_2$ after detachment. Active regions of PL spectra are fitted with mixed Gaussian-Lorentzian function.

[$I(A)/I(A^-)$] of $A$ and $A^-$ is doubled after the detachment. The increase in free-exciton emission intensity is attributed partly to the decrease in the electron-carrier density and partly to the conversion of bound excitons to free excitons after detachment. It is well known that the $SiO_2$ substrate induces the $n$-type doping to $MoS_2$ flakes [2,26]. Thus, detachment from the $SiO_2$ substrate reduces native electron-carrier density. As a result, free excitons are stabilized, and nonradiative recombination is significantly suppressed because of low carrier density [26].

Exciton-peak analysis revealed the stabilization of free-exciton emission after the detachment. It was attributed to the reduction of native electron-carrier density because of the absence of $n$-type doping originating from substrate-borne impurities. RT Raman and PL analysis were further carried out to elucidate the carrier-density variation before and after the detachment of the flake [Fig. 5]. The electron-carrier density of 1L-$MoS_2$ can be analyzed qualitatively by $A_{1g}$ phonon mode [55,56]. The $A_{1g}$ mode softens with increasing electron doping [55,56]. An optical micrograph of the given 1L-$MoS_2$ flake is shown in the inset of Fig. 5(a). The inset of Fig. 5(b) shows the low-temperature PL spectrum of the flake after detachment. The absence of bound exciton emission confirms the detachment of 1L-$MoS_2$ from the $SiO_2$ substrate [inset of Fig. 5(b)]. RT Raman spectra of 1L-$MoS_2$ flake before and after detachment are shown in Fig. 5(a). The peak positions of Raman modes were obtained by fitting the active region using the Lorentzian function. The frequency of $A_{1g}$ mode before and after detachment was found to be 404.1 and 404.9 $cm^{-1}$, respectively, and the $E^1_{2g}$ mode frequency was found to be 384.8 and 385.7 $cm^{-1}$ before and after detachment, respectively. In other words, both modes were blueshifted after the detachment. However, the $A_{1g}$ phonon-mode frequency exclusively depends on the carrier density due to stronger electron-phonon coupling [55]. In contrast, the frequency of the $E^1_{2g}$ mode is influenced by the in-plane strain. The blueshift of $A_{1g}$ phonon mode by 0.8 $cm^{-1}$ after detachment confirms the reduction of electron-carrier density in the flake. Subsequently, the RT PL spectrum of 1L-$MoS_2$ before and after detachment was compared [Fig. 5(b)]. The total peak intensity was enhanced by ∼100% after detachment [Fig. 5(b)]. Figure S7 shows the fitting results of RT PL spectrum before and after detachment [44]. The $A$-exciton emission was negligible in as grown 1L-$MoS_2$ flake. $I(A)/I(A-)$ was found to be 0.02 and increased to 0.39 after the detachment. In other words, 20 times increment was observed in $I(A)/I(A^-)$ after the detachment. The increase of $I(A)/I(A^-)$ reveals the stabilization of free excitons after the detachment. However, the peak

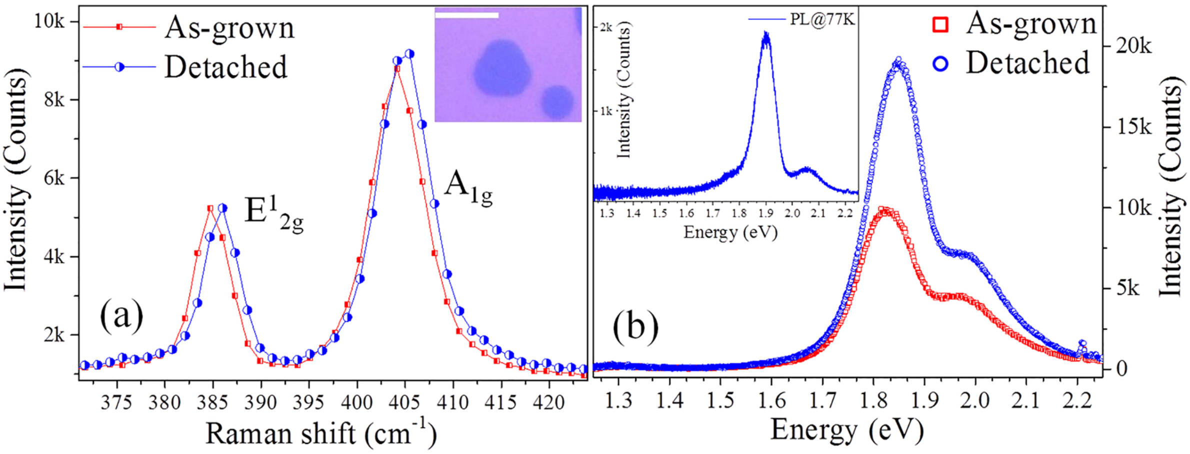

FIG. 5. (a) RT Raman spectra of as-grown and detached flake. Inset figure shows optical micrograph of given flake. Scale bar: 10 μm. (b) RT PL spectra of monolayer 1L-$MoS_2$ flake before and after detachment. Inset of (b) shows PL spectrum of detached flake recorded at sample-stage temperature of 77 K.

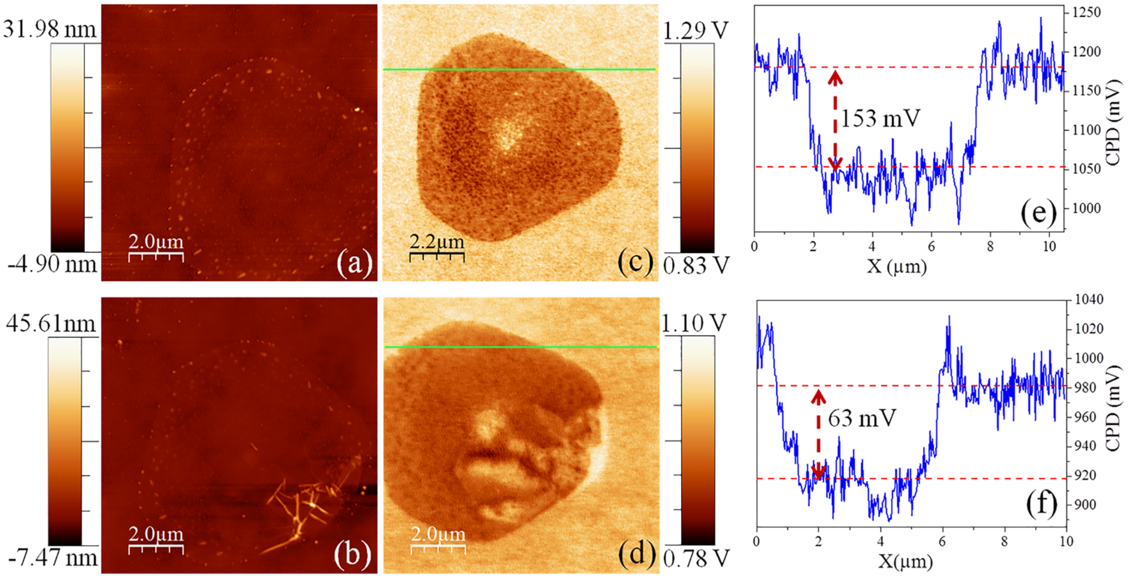

FIG. 6. AFM image of 1L-$MoS_2$ flake: (a) before and (b) after detachment. Topographic modulations are clearly observed in detached flake (b). CPD or SP map of 1L-$MoS_2$ flake: (c) before and (d) after detachment. (e) Line profile of CPD map (c) of as-grown 1L-$MoS_2$ flake. (f) Line profile of CPD map (d) of 1L-$MoS_2$ flake after detachment. Line profiles were acquired along green lines shown in (c) and (d).

positions of $A^-$, $A$, and $B$ were not shifted after detachment. The stabilization of free-exciton emission arises because of reduced carrier density after detachment. In addition, the integrated intensity of individual peaks corresponding to $A^-$, $A$, and $B$ also increased significantly after the detachment. The enhancement of overall PL intensity is attributed to the significant suppression of Auger recombination because of reduced carrier density after detachment [27].

As of now, the detachment of the flake from the substrate was confirmed by spectroscopic analysis. The structural integrity of the detached flake was further studied by AFM. The topographic images of as-grown and detached flakes are shown in Figs. 6(a) and 6(b), respectively. The optical micrograph of the given flake is shown in the inset of Fig. 5(a). AFM image [Fig. 6(b)] of detached flake clearly shows topographic modifications compared to that for the as-grown flake. One of the edge regions of the detached flake has shown sharp streaks [Fig. 6(b)]. These nanowire-like streaks are nothing but wrinkles formed after the detachment. Usually, wrinkles were found in wet-transferred flakes. Thus, the observed wrinkles confirm the detachment of the flake from the substrate.

Work function ($\phi$) is an intrinsic property of the material which can be correlated with the carrier density of the material. In principle, the work function is the minimum energy required to bring an electron to the vacuum level from the Fermi level ($E_F$). The position of $E_F$ varies with the variation of carrier densities in the material. In a relative comparison, any change in the work function indicates a change in the carrier density of the material, as it dictates the position of the $E_F$. However, if the defects act as dopants, a change in the carrier density is expected with the variation of defect density. Thus, the change in work function indirectly reveals the change in the defect density [57]. KPFM is one of the techniques to measure the work function of materials with high energy (~10 meV) and spatial resolutions (~10 nm) [57,58]. Here, KPFM measurements were carried out on the 1L-$MoS_2$ flake before and after detachment. As the measurements were carried out with the same tip, the work function of the 1L-$MoS_2$ flakes was estimated by using the $SiO_2$ substrate work function (5.05 eV) [59], $\phi_{MoS2} = \phi_{SiO2} - e[(V_{CPD})_{SiO2} - (V_{CPD})_{MoS2}]$, where $V_{CPD}$ is a contact potential difference (CPD) between tip and sample or surface potential (SP) of sample and $e$ is the elementary charge. A detailed derivation of $\phi_{MoS2}$ is provided in the SM [44]. Figures 6(c) and 6(d) show the SP maps of the 1L-$MoS_2$ flake before and after detachment. Both cases showed that the SP of $SiO_2$ substrates was greater than 1L-$MoS_2$ flake. It was found that the SP of the as-grown flake [Fig. 6(c)] was uniform throughout the flake. However, SP of detached flake [Fig. 6(d)] was found to be nonuniform. Interestingly, the change in the SP was observed in a region where wrinkles were formed. Thus, the nonuniform distribution of SP of detached flakes is attributed to the wrinkles formed after the detachment. The SP of 1L-$MoS_2$ and $SiO_2$ was estimated by using the line profiles acquired from the CPD maps. The line profiles were obtained along the green lines shown in Figs. 6(c) and 6(d). These line profiles were taken in precisely the exact position of the flake before and after detachment. The line profiles of CPD are represented in Figs. 6(e) and 6(f) for the as-grown and detached flake, respectively. The SP difference between $SiO_2$ and as-grown 1L-$MoS_2$ flake is ~153 mV [Fig. 6(e)], whereas it is 63 mV for the detached flake [Fig. 6(f)]. The calculated work function of the as-grown and detached 1L-$MoS_2$ flake is 4.897 and 4.987 eV, respectively. The work function of 1L-$MoS_2$ flake was increased by 90 meV after the detachment. In other words, $E_F$ shifts downwards by 90 meV after the detachment. In general, the carrier density in semiconducting material dictates the $E_F$ position. In the case of $n$-type material, $E_F$ rises with increased electron-carrier density. In the present case, the downshift

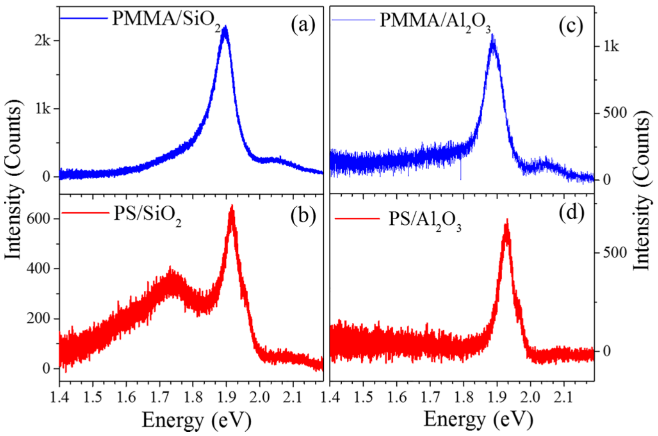

FIG. 7. Low-temperature PL studies on 1L-MoS$_2$ flakes ($\leqslant$30 μm$^2$) transferred onto another SiO$_2$ and sapphire substrates. PL spectra were recorded by maintaining sample-stage temperature at 77 K. (a) PL spectrum of 1L-MoS$_2$ flake transferred by PMMA polymer. b) PL spectrum of 1L-MoS$_2$ flake transferred by PS polymer. PL spectrum of 1L-MoS$_2$ flake transferred onto sapphire substrate with (c) PMMA and (d) PS polymer.

of $E_F$ must be originated from the reduced electron-carrier density due to the absence of $n$-type doping by substrate-borne impurities. Thus, KPFM analysis further reiterates that defect density, which originates from the substrate or substrate-borne impurities, is reduced in detached flakes. Here, our results once again confirm that the SiO$_2$ substrate induces $n$-type doping to monolayer MoS$_2$.

### C. Bound exciton emission in polymer-assisted transferred 1L-MoS$_2$ flakes

We also investigated low-temperature (77 K) PL emission properties of 1L-MoS$_2$ flakes transferred by polymer-assisted techniques such as the PMMA-assisted wet-transfer method [41] and surface-energy assisted method. In the surface-energy assisted method, PS was used as the carrier polymer [43]. Now onwards, the flakes transferred by the wet-transfer method and surface-energy assisted method are termed PMMA-transferred and PS-transferred flakes, respectively. As-grown 1L-MoS$_2$ flakes were transferred onto another SiO$_2$ substrate to see the exclusive transfer effects. Figures 7(a) and 7(b) show the PL spectra of PMMA-transferred and PS-transferred 1L-MoS$_2$ flake ($\leqslant$ 30 μm$^2$) supported by SiO$_2$ substrate, respectively. The additional data are shown in Fig. S8 [44]. Interestingly, the bound exciton emission was observed in PS-transferred flakes only [Fig. 7(b)]. Earlier, the absence of bound exciton emission in PMMA-transferred flakes was attributed to the passivation of S vacancies by KOH during the transfer process [37]. However, our study indicated that the bound exciton emission originated from substrate-borne impurities. Thus, the absence of bound exciton emission in PMMA-transferred flakes cannot be attributed to the passivation of S vacancies alone. In other words, bound exciton emission could be absent in PMMA-transferred flakes because of the detachment of flakes from the SiO$_2$ substrate. The origin of bound exciton emission in PS-transferred flakes can be understood by analyzing the doping effects of PS and PMMA polymer. It is worth mentioning that PS induces $n$-type doping [56], and PMMA induces $p$-type doping to 1L-MoS$_2$ [41]. The doping analysis was carried out by evaluating the trion- and free-exciton integrated intensities (Fig. S9 [44]). Trion emission dominated over free-exciton emission in PS-transferred flakes. In contrast, free-exciton emission dominated the trion emission in PMMA-transferred flakes. Thus, it indicated that PS-transferred flakes were $n$-type doped. In this context, the observation of bound exciton emission only in SiO$_2$-supported PS-transferred flakes suggests that excitons are preferably bound to impurities that can act as $n$-type dopants, as in the case of substrate-borne impurities. In addition, it was also found that the PL intensity of PS-transferred flakes was considerably lower than that of PMMA-transferred flakes. The low PL intensity of PS transferred flake can be attributed to the $n$-type doping of PS polymer [56]. In contrast, the relatively high PL intensity of PMMA-transferred flakes is attributed to $p$-type doping by the PMMA [41].

Furthermore, we transferred the as-grown flakes onto the sapphire substrate by the above-mentioned methods. Subsequently, we carried out the low-temperature PL (77 K) measurements on small-area flakes ($\leqslant$30 μm$^2$). Figures 7(b) and 7(c) show the low-temperature PL spectrum of PMMA- and PS-transferred flakes supported by the sapphire substrate, respectively. Surprisingly, the bound exciton emission was absent in both cases. This observation can be understood by invoking the doping effects of substrate-borne moisture. In transferred flakes, substrate-borne moisture acts as an $n$-type dopant for 1L-MoS$_2$. It was demonstrated that the doping effect by substrate-borne moisture is considerably stronger than that from the substrate [56]. Moreover, the $n$-type doping by substrate-borne moisture is significantly higher than that of doping by substrate and PS polymer [56]. It is worth mentioning that the intrinsic moisture-attracting property of the substrates dictates the amount of trapped moisture. It was reported that the amount of trapped moisture was significantly higher in SiO$_2$-supported flakes than in sapphire-supported flakes [56]. Thus, the PS-transferred flakes supported by the sapphire substrate are less doped than the SiO$_2$-supported flakes. The bound exciton emission may be absent because of considerable low $n$-type doping in sapphire-supported flakes. The bound exciton emission in PS-transferred flakes supported by SiO$_2$ substrate might be originated from heavy doping of substrate-borne moisture. However, further investigations are required to authenticate the observed results.

## IV. DISCUSSION

As mentioned in the Introduction, bound exciton emission was attributed to the excitons bound to sulfur vacancies ($V_S$ and $V_{2S}$) in earlier studies [35,37]. In the present study, we found that the bound exciton emission was absent in the case of dry detached 1L-MoS$_2$ flakes. As we have not used any passivation methods, one cannot expect the passivation of S vacancies in this approach. We carried out the low-temperature measurements after keeping the sample in a vacuum for 1 day and ambient conditions for 5 days. Subsequently, we measured low-temperature PL after heating the sample to a moderate temperature on a hot plate. In all these cases, we could not revive the bound exciton emission in the detached flake (not shown in the figure). The bound exciton emission can be revived by these methods if it is absent because of the passivation of S vacancies in the ambient conditions. Thus, one can rule out the role of S-vacancy passivation in the absence of bound exciton emission after detachment. The bound exciton emissions must be originated from substrate-borne impurities. In addition, the detached flake contains a relatively low electron-carrier density compared to that of the as-grown flake. Thus, the substrate-borne defects act as *n*-type dopants. Typical impurities found on the $SiO_2$ surface are H, Na, and K, which may be adsorbed during the oxidation process [60,61]. Moreover, Na is a representative impurity in the $SiO_2$ oxide layer, which is usually incorporated during the oxidation process. Dolui *et al.* [61] performed the *ab initio* density-functional theory (DFT) calculations to study the electronic properties of $MoS_2$ deposited on $SiO_2$ substrates. It was found that the Na impurities and O dangling bonds introduce the localized states which influence the conductivity of the flake. DFT calculations revealed that Na acted as a shallow donor with small activation energy, whereas oxygen dangling bonds made the system *p* type. In contrast, H adsorption forms deep-level states, which cannot modify the conductivity of the material because of high activation energy. Thus, in the present case, bound exciton emission can be attributed to substrate-borne impurities like Na because it acts as an *n*-type dopant. Moreover, we cannot ascribe the bound exciton emission to O dangling bonds because of its *p*-type doping nature. Our results indicate that the origin of bound exciton emission in the CVD-grown monolayer $MoS_2$ is completely different compared to that for the exfoliated monolayer $MoS_2$. Interestingly, bound exciton emission is only observed in heavily doped *n*-type 1L-$MoS_2$ systems.

## V. CONCLUSION

In summary, an innovative dry-detachment method without any polymer usage was adopted to delineate the origin of bound exciton emission in CVD-grown monolayer $MoS_2$. This approach is based on the differential thermal expansion coefficients of $MoS_2$ and $SiO_2$ substrate. The bound exciton emission was completely absent in detached monolayer flakes. Thus, bound exciton emission is attributed to free excitons bound to $SiO_2$ substrate-borne impurities. The electron-carrier density of monolayer $MoS_2$, which was confirmed by Raman and photoluminescence spectroscopy, was marginally reduced after detachment. In addition, the increased work function of the detached flake by 90 meV further confirmed the reduced carrier density indicating *n* doping of the $SiO_2$ substrate. Our results reveal that the substrate plays the dominant role in defect-bound exciton emission in CVD-grown monolayer $MoS_2$ which has been overlooked so far. The comparative PL analysis with wet-transferred flakes revealed that bound excitons are preferably bound to *n*-type impurities. Furthermore, bound exciton emission contribution was found to depend on the area of the flake. Bound exciton emission was observed even at 210 K in large-area flakes because of reduced laser-induced heating effects. The present findings emphasize the importance of substrate-borne impurities in monolayer $MoS_2$ which may apply to other 2D semiconductor materials deposited by CVD.

---

[1] C. Lee, H. Yan, L. E. Brus, T. F. Heinz, J. Hone, and S. Ryu, ACS Nano **4**, 2695 (2010).

[2] K. F. Mak, C. Lee, J. Hone, J. Shan, and T. F. Heinz, Phys. Rev. Lett. **105**, 136805 (2010).

[3] A. Splendiani, L. Sun, Y. Zhang, T. Li, J. Kim, C.-Y. Chim, G. Galli, and F. Wang, Nano Lett. **10**, 1271 (2010).

[4] A. D. Platt, M. J. Kendrick, M. Loth, J. E. Anthony, and O. Ostroverkhova, Phys. Rev. B **84**, 235209 (2011).

[5] A. V. Kolobov and J. Tominaga, *Two-Dimensional Transition-Metal Dichalcogenides* (Springer, Switzerland, 2016).

[6] T. C. Berkelbach, M. S. Hybertsen, and D. R. Reichman, Phys. Rev. B **88**, 045318 (2013).

[7] A. Chernikov, T. C. Berkelbach, H. M. Hill, A. Rigosi, Y. Li, B. Aslan, D. R. Reichman, M. S. Hybertsen, and T. F. Heinz, Phys. Rev. Lett. **113**, 076802 (2014).

[8] Y. Yu, A. W. Bataller, R. Younts, Y. Yu, G. Li, A. A. Puretzky, D. B. Geohegan, K. Gundogdu, and L. Cao, ACS Nano **13**, 10351 (2019).

[9] K. F. Mak, K. He, C. Lee, G. H. Lee, J. Hone, T. F. Heinz, and J. Shan, Nat. Mater. **12**, 207 (2013).

[10] Y. You, X.-X. Zhang, T. C. Berkelbach, M. S. Hybertsen, D. R. Reichman, and T. F. Heinz, Nat. Phys. **11**, 477 (2015).

[11] D. K. Zhang, D. W. Kidd, and K. Varga, Nano Lett. **15**, 7002 (2015).

[12] J. Pei, J. Yang, X. Wang, F. Wang, S. Mokkapti, T. Lu, J. Zheng, Q. Qin, D. Neshev, H. Tan *et al.*, ACS Nano **11**, 7468 (2017).

[13] J. Pandey and A. Soni, Appl. Surf. Sci. **463**, 52 (2019).

[14] O. Lopez-Sanchez, D. Lembke, M. Kayci, A. Radenovic, and A. Kis, Nat. Nanotechnol. **8**, 497 (2013).

[15] F. Koppens, T. Mueller, P. Avouris, A. Ferrari, M. Vitiello, and M. Polini, Nat. Nanotechnol. **9**, 780 (2014).

[16] M. M. Furchi, D. K. Polyushkin, A. Pospischil, and T. Mueller, Nano Lett. **14**, 6165 (2014).

[17] B. Radisavljevic, A. Radenovic, J. Brivio, V. Giacometti, and A. Kis, Nat. Nanotechnol. **6**, 147 (2011).

[18] D. Jariwala, V. K. Sangwan, L. J. Lauhon, T. J. Marks, and M. C. Hersam, ACS Nano **8**, 1102 (2014).

[19] M. Bernardi, M. Palummo, and J. C. Grossman, Nano Lett. **13**, 3664 (2013).

[20] H. Li, Z. Yin, Q. He, H. Li, X. Huang, G. Lu, D. Fam, A. Tok, Q. Zhang, and H. Zhang, Small **8**, 63 (2012).

[21] S. Tongay, J. Suh, C. Ataca, W. Fan, A. Luce, J. S. Kang, J. Liu, C. Ko, R. Raghunathanan, J. Zhou *et al.*, Sci. Rep. **3**, 2657 (2013).

[22] P. K. Chow, R. B. Jacobs-Gedrim, J. Gao, T.-M. Lu, B. Yu, H. Terrones, and N. Koratkar, ACS Nano **9**, 1520 (2015).

[23] S. Deb, P. Chakrabarti, P. K. Mohapatra, B. K. Barick, and S. Dhar, Appl. Surf. Sci. **445**, 542 (2018).

[24] K. Greben, S. Arora, M. G. Harats, and K. I. Bolotin, Nano Lett. **20**, 2544 (2020).

[25] P. Johari and V. B. Shenoy, ACS Nano **6**, 5449 (2012).

[26] N. Scheuschner, O. Ochedowski, A.-M. Kaulitz, R. Gillen, M. Schleberger, and J. Maultzsch, Phys. Rev. B **89**, 125406 (2014).

[27] Y. Sun, R. Wang, and K. Liu, Appl. Phys. Rev. **4**, 011301 (2017).

[28] S. Mouri, Y. Miyauchi, and K. Matsuda, Nano Lett. **13**, 5944 (2013).

[29] M. Amani, D. Lien, D. Kiriya, J. Xiao, A. Azcatl, J. Noh, S. R. Madhvapathy, R. Addou, S. KC, M. Dubey *et al.*, Science **350**, 1065 (2015).

[30] W. Su, H. Dou, D. Huo, N. Dai, and L. Yang, Chem. Phys. Lett. **635**, 40 (2015).

[31] K. K. Madapu, C. A. Bhuyan, S. Srivastava, and S. Dhara, J. Mater. Chem. C **9**, 3578 (2021).

[32] C. A. Bhuyan, K. K. Madapu, and S. Dhara, J. Appl. Phys. **132**, 204303 (2022).

[33] T. Korn, S. Heydrich, M. Hirmer, J. Schmutzler, and C. Schüller, Appl. Phys. Lett. **99**, 102109 (2011).

[34] G. Plechinger, F. X. Schrettenbrunner, J. Eroms, D. Weiss, C. Schueller, and T. Korn, Phys. Status Solidi RRL **6**, 126 (2012).

[35] N. Saigal and S. Ghosh, Appl. Phys. Lett. **109**, 122105 (2016).

[36] J. Klein, A. Kuc, A. Nolinder, M. Altzschner, J. Wierzbowski, F. Sigger, F. Kreupl, J. J. Finley, U. Wurstbauer, A. W. Holleitner *et al.*, 2D Mater. **5**, 011007 (2017).

[37] T. Verhagen, V. L. Guerra, G. Haider, M. Kalbac, and J. Vejpravova, Nanoscale **12**, 3019 (2020).

[38] S. V. Sivaram, A. T. Hanbicki, M. R. Rosenberger, G. G. Jernigan, H.-J. Chuang, K. M. McCreary, and B. T. Jonker, ACS Appl. Mater. Interfaces **11**, 16147 (2019).

[39] W. Li, A. G. Birdwell, M. Amani, R. A. Burke, X. Ling, Y. H. Lee, X. Liang, L. Peng, C. A. Richter, J. Kong *et al.*, Phys. Rev. B **90**, 195434 (2014).

[40] T. T. Tran, K. Bray, M. J. Ford, M. Toth, and I. Aharonovich, Nat. Nanotechnol. **11**, 37 (2016).

[41] C. A. Bhuyan, K. K. Madapu, K. Prabakar, A. Das, S. Polaki, S. K. Sinha, and S. Dhara, Adv. Mater. Interfaces **9**, 2200030 (2022).

[42] K. K. Madapu and S. Dhara, AIP Adv. **10**, 085003 (2020).

[43] A. Gurarslan, Y. Yu, L. Su, Y. Yu, F. Suarez, S. Yao, Y. Zhu, M. Ozturk, Y. Zhang, and L. Cao, ACS Nano **8**, 11522 (2014).

[44] See Supplemental Material at http://link.aps.org/supplemental/10.1103/PhysRevB.108.085429 for the optical micrographs of as-grown monolayer $MoS_2$ flakes; statistical data of low-temperature photoluminescence spectra; and fitted room-temperature PL spectra of small- and large-area flakes; temperature-dependent PL analysis of small- and large-area flakes; derivation of the monolayer $MoS_2$ work function from the KPFM results; and description of mixed Gaussian-Lorentzian function. It also contains Refs. [45–51].

[45] A. L. Stancik and E. B. Brauns, Vib. Spectrosc. **47**, 66 (2008).

[46] X. Ling, Y.-H. Lee, Y. Lin, W. Fang, L. Yu, M. S. Dresselhaus, and J. Kong, Nano Lett. **14**, 464 (2014).

[47] Y. Lin, X. Ling, L. Yu, S. Huang, A. L. Hsu, Y.-H. Lee, J. Kong, M. S. Dresselhaus, and T. Palacios, Nano Lett. **14**, 5569 (2014).

[48] D. Kaplan, Y. Gong, K. Mills, V. Swaminathan, P. Ajayan, S. Shirodkar, and E. Kaxiras, 2D Mater. **3**, 015005 (2016).

[49] J. Gao, B. Li, J. Tan, P. Chow, T.-M. Lu, and N. Koratkar, ACS Nano **10**, 2628 (2016).

[50] V. Jain, M. C. Biesinger, and M. R. Linford, Appl. Surf. Sci. **447**, 548 (2018).

[51] K. Saito, M. Okada, R. Kitaura, H. Kishida, and T. Koyama, Phys. Rev. B **103**, L201401 (2021).

[52] C. Sevik, Phys. Rev. B **89**, 035422 (2014).

[53] A. Sinha, H. Levinstein, and T. Smith, J. Appl. Phys. **49**, 2423 (1978).

[54] P. Gant, P. Huang, D. P. de Lara, D. Guo, R. Frisenda, and A. Castellanos-Gomez, Mater. Today **27**, 8 (2019).

[55] B. Chakraborty, A. Bera, D. V. S. Muthu, S. Bhowmick, U. V. Waghmare, and A. K. Sood, Phys. Rev. B **85**, 161403(R) (2012).

[56] Y. Yu, Y. Yu, C. Xu, Y. Q. Cai, L. Su, Y. Zhang, Y. W. Zhang, K. Gundogdu, and L. Cao, Adv. Funct. Mater. **26**, 4733 (2016).

[57] X. Wang, J. Dan, Z. Hu, J. F. Leong, Q. Zhang, Z. Qin, S. Li, J. Lu, S. J. Pennycook, W. Sun *et al.*, Chem. Mater. **31**, 7970 (2019).

[58] K. K. Madapu, S. Parida, K. Jeganathan, M. Baral, and S. Dhara, J. Appl. Phys. **125**, 164308 (2019).

[59] S. Choi, Z. Shaolin, and W. Yang, J. Korean Phys. Soc. **64**, 1550 (2014).

[60] E. A. Irene, Crit. Rev. Solid State Mater. Sci. **14**, 175 (1988).

[61] K. Dolui, I. Rungger, and S. Sanvito, Phys. Rev. B **87**, 165402 (2013).